Photonuclear Data Evaluation of Actinides

I. Raškinytė*, E. Dupont*, B. Morillon† and D. Ridikas*

*Commissariat à l'Energie Atomique, CEA/Saclay, DSM/DAPNIA/SPhN, Gif-sur-Yvette, France
†Commissariat à l'Energie Atomique, CEA/DAM–Ile de France, DAM/DPTA/SPN, Bruyères-le-Châtel, France

Abstract. There is a renewed interest in photonuclear reactions for various applications such as radioactive ion beam or neutron production, waste transmutation and detection of nuclear materials. However, contrary to the neutron induced reactions, evaluated nuclear data files for photons contain little information, especially for incident energies above 20 MeV. From a physics point of view, gamma induced reactions allow to study nuclear reaction mechanisms for some compound nucleus hardly available with a direct neutron probe. This paper gives an overview of our on-going activities on photonuclear data evaluation of uranium and thorium isotopes.

1. INTRODUCTION

Nuclear data of photo-induced reactions are important for a variety of present or emerging applications. Among them are radiation transport simulation and radiation shielding design of accelerators or innovative reactors, activation analysis, safeguards and inspection technologies, nuclear waste transmutation. In terms of incident energies, the giant dipole resonance region below 30 MeV is essential for most applications. In addition, some medical applications request photonuclear data up to 50 MeV. Finally, it is also desirable to have evaluated photonuclear data up to 130 MeV for the simulation of intense neutron sources and to complement the neutron and proton high-energy libraries.

Actinide cross-section evaluations were reviewed in the framework of a specific IAEA coordinated research project [1]. Recently, major actinide cross sections and spectra were evaluated in the framework of a collaboration between LANL and CEA [2]. These evaluations were done for incident photon energies below 20 MeV.

The present work aims at the extension of actinide evaluations up to 130 MeV. This paper presents on-going evaluation activity for ^{235}U and ^{232}Th. Recent measurements of delayed neutron yields performed at CEA [3] will complement this evaluation effort and the outcome will be proposed for insertion into the Joint Evaluated Fission and Fusion (JEFF) library to answer application needs.

2. NUCLEAR REACTION MODELS

In a photoreaction, the target nucleus is directly excited by the incident photon. Below a few tens of MeV, the main decay channels are fission and neutron emission only because of the high Coulomb barrier of heavy nuclei. However, light charged particle emission may be significant at higher energy. Depending on their remaining excitation energy, the residual nuclei can further emit particles or undergo fission.

In this work, the photoabsorption process is described by the giant dipole resonance and quasideuteron mechanisms. Preequilibrium particle emissions are treated with the classical exciton model. At equilibrium, the compound nucleus decay channels are handled within the Hauser-Feshbach statistical model. Neutron transmission coefficients are calculated with a coupled-channel optical model and fission transmission coefficients are calculated with a double humped parabolic model. These calculations are performed with the TALYS code [4], which includes all above mentioned nuclear reaction models. The prompt fission neutron emission is treated within the Madland-Nix model [5].

2.1. Photoabsorption

When modeling photon induced reactions, the first step is the determination of the photoabsorption cross section. At low energies, below about 30 MeV, the giant dipole resonance (GDR) is the dominant excitation mechanism. At higher energies, up to 150 MeV (pion threshold), the phenomenological model of photoabsorption on a neutron-proton pair (quasideuteron, QD) becomes dominant.

Following Chadwick *et al.* [6], the photoabsorption cross section is given by

$$\sigma_{abs}(E_\gamma) = \sigma_{GDR}(E_\gamma) + \sigma_{QD}(E_\gamma). \tag{1}$$

In the case of deformed nuclei, the GDR component is given as a sum of two Lorentzians

$$\sigma_{GDR}(E_\gamma) = \sum_{i=1,2} \sigma_{E1,i} \frac{E_\gamma^2 \Gamma_{E1,i}^2}{(E_\gamma^2 - E_{E1,i}^2)^2 + E_\gamma^2 \Gamma_{E1,i}^2}, \tag{2}$$

where $\sigma_{E1,i}$, $E_{E1,i}$, $\Gamma_{E1,i}$ are the GDR peak cross section, energy position and width respectively.

The QD component is taken from the model of Chadwick *et al.* [6]. It relates the photoabsorption cross section to the experimental deuteron photodisintegration cross section $\sigma_d(E_\gamma)$,

$$\sigma_{QD}(E_\gamma) = \frac{L}{A} NZ \sigma_d(E_\gamma) f(E_\gamma), \tag{3}$$

where L is the Levinger parameter [7] and $f(E_\gamma)$ is the Pauli-blocking function. See reference [6] for more details.

2.2. Compound Nucleus

In the statistical approach, the competition between all decay channels involves major ingredients such as nuclear level density and transmission coefficients through optical model potential or fission barrier. The following paragraphs shortly describe the models used to calculate these physical quantities.

2.2.1. Level Density

The TALYS code includes several level density models. Present calculations were done using the Gilbert-Cameron composite formula [8] with energy-dependent level density parameter [9].

In the Gilbert-Cameron level density formulation, the excitation energy range is divided in a low energy part from zero to a matching energy E_M and a high energy part above E_M

$$\rho(E_{ex}) = \begin{cases} \rho_T(E_{ex}), & E_{ex} \le E_M \\ \rho_F(E_{ex}), & E_{ex} > E_M. \end{cases} \tag{4}$$

At low excitation energy, the model is based on the experimental evidence that the cumulative number of the first discrete levels *vs.* energy can be well reproduced by a constant-temperature law. Accordingly, the constant temperature part of the total level densities is given by

$$\rho_T(E_{ex}) = \frac{1}{T} \exp \frac{E_{ex} - E_0}{T}, \tag{5}$$

where the nuclear temperature T and E_0 are adjustable parameters.

For higher energies, the Fermi-gas model is more suitable and the total level density is then given by

$$\rho_F(E_{ex}) = \frac{\sqrt{\pi}}{12} \frac{\exp(2\sqrt{aU})}{\sqrt{2\pi}\sigma a^{1/4} U^{5/4}}, \tag{6}$$

where $U = E_{ex} - \Delta$, σ^2 is the spin cut-off factor and a is the level density parameter. In our calculations we used Ignatyuk [9] level density parameter formula

$$a = \tilde{a} \left[1 + \delta W \frac{1 - \exp(-\gamma U)}{U} \right]. \tag{7}$$

The pairing energy Δ, the asymptotic level density value $\tilde{a}$, the shell damping parameter γ and the shell correction energy δW are deduced from systematics [4]. The expressions for ρ_T and ρ_F are matched by requiring the continuity

of the function $\rho(E_{ex})$ and its derivative at the energy E_M. Another constraint is given by considering that the constant-temperature law should reproduce the experimental discrete levels from a lower level N_{low} to an upper level N_{top}. These levels should be chosen such that $\rho_T(E_{ex})$ optimally describes the observed discrete states. In default TALYS calculations $N_{low} = 2$ and N_{top} is determined from microscopic level densities.

2.2.2. Neutron Emission

Thanks to the time-reversal invariance of nuclear reactions, the neutron exit channel in the (γ, n) reaction shares the same nuclear parameters as the entrance channel of the (n, γ) reaction. Therefore, transmission coefficients for the exit channel are calculated with a global coupled-channels optical potential developed for neutron-actinide interaction from 1 keV to 200 MeV by Soukhovitskii *et al.* [10]. Coupling between levels in coupled-channel calculations is due to the deformed nuclear optical potential, where deformation is taken into account through the deformed nuclear shapes

$$R(\theta', \varphi') = R_0 \left\{ 1 + \sum_{\lambda=2,4,6} \beta_{\lambda 0} Y_{\lambda 0}(\theta', \varphi') \right\}, \tag{8}$$

where $Y_{\lambda 0}$ are spherical harmonics and (θ', φ') are angular coordinates in the body-fixed frame. The optical potential is of a standard Wood-Saxon shape with real and imaginary volume, imaginary surface and real and imaginary spin-orbit terms given by [10]

$$\begin{aligned}
-V_R f_R(r, R(\theta', \varphi')) &\qquad \text{real volume (R)} \\
-iW_V f_V(r, R(\theta', \varphi')) &\qquad \text{imaginary volume (V)} \\
i4W_D a_D \frac{d}{dr} f_D(r, R(\theta', \varphi')) &\qquad \text{imaginary surface (D)} \\
\left(\frac{\hbar}{m_\pi c}\right)^2 V_{so} \frac{1}{r} \frac{d}{dr} f_{so}(r, R(\theta', \varphi')) \hat{\sigma} \cdot \hat{L} &\qquad \text{real spin-orbit (so)} \\
i \left(\frac{\hbar}{m_\pi c}\right)^2 W_{so} \frac{1}{r} \frac{d}{dr} f_{so}(r, R(\theta', \varphi')) \hat{\sigma} \cdot \hat{L} &\qquad \text{imaginary spin-orbit (so),}
\end{aligned} \tag{9}$$

with the form factors given as

$$f_i(r) = \left[1 + exp((r - R_i(\theta', \varphi'))/a_i)\right]^{-1}, \qquad i = R, V, D, so. \tag{10}$$

Deformed radii R_i are given by equation (8) with $R_0 = r_i A^{1/3}$. However, the spin-orbit term is not deformed in standard TALYS calculations and in that particular case $R(\theta', \varphi') = R_0$. Well depths V_i as well as r_R are energy dependent. Their functional dependence as well as values of r_i and a_i are described in the reference [10]. In the latter work, the optical potential parameters were searched for to reproduce available neutron- and proton-induced cross sections for ^{238}U and ^{232}Th. Afterwards, these parameters were used to calculate cross sections of other actinides like ^{233}U and ^{235}U. On the contrary, the deformation parameters were adjusted for each actinide.

2.2.3. Fission Channel

In this work, fission transmission coefficients were calculated using a double humped barrier model. The Hill-Wheeler expression gives the quantum penetrability through a fission barrier described by an inverted parabola

$$T_{HW}(E_{ex}) = \left[1 + exp\left(-2\pi \frac{E_{ex} - B_f}{\hbar\omega}\right)\right]^{-1}, \tag{11}$$

where B_f is the barrier height relative to the nucleus ground state and $\hbar\omega$ is the barrier curvature.

For a transition state of energy ε_i above the top of the barrier, one simply assumes the barrier is shifted up by ε_i

$$T_{HW}(E_{ex},\varepsilon_i) = \left[1+exp\left(-2\pi\frac{E_{ex}-B_f-\varepsilon_i}{\hbar\omega}\right)\right]^{-1}. \tag{12}$$

For a compound nucleus with excitation energy E_{ex}, spin J, and parity Π, the total fission transmission coefficient is the sum of the individual transmission coefficients for each barrier through which the nucleus may tunnel

$$T_f^{J,\Pi}(E_{ex}) = \sum_i T_{HW}(E_{ex},\varepsilon_i) f(i,J,\Pi) + \int_{E_{th}}^{E_{ex}} \rho(\varepsilon,J,\Pi) T_{HW}(E_{ex},\varepsilon) d\varepsilon. \tag{13}$$

The summation runs over all discrete transition states on top of the barrier and E_{th} marks the beginning of the continuum. $f(i,J,\Pi) = 1$, if the spin-parity of the transition state equal that of the compound nucleus and 0 otherwise. Moreover, $\rho(\varepsilon,J,\Pi)$ are the level densities at an excitation energy ε of the fission channels with spin J and parity Π.

In the case of a double-humped barriers A and B, one assumes that tunneling through the barriers can be separated into two steps. One first should know the probability to cross the first barrier and then multiply it by the probability to fission. Consequently the effective fission transmission coefficient is given by

$$T_{eff}^{J\Pi} = \frac{T_A^{J\Pi} T_B^{J\Pi}}{T_A^{J\Pi} + T_B^{J\Pi}}. \tag{14}$$

2.3. Fission Neutrons

In the present work, one considers only prompt fission neutrons evaporated from the primary fragments. A study of the delayed photofission neutron yields is described in a companion paper [3].

2.3.1. Prompt Neutrons

The prompt fission neutron multiplicity and spectra are calculated using the Los Alamos model initially proposed by Madland and Nix [5], and further developped by Vladuca and Tudora [11].

At high excitation energy, the competition between multiple-chance fission (γ, xnf) is taken into account and the xn neutrons emitted prior to scission are also considered. However, the pre-equilibrium effects are neglected and neutron emission is based on the nuclear evaporation theory only.

The distribution of the fission-fragment residual temperature is assumed triangular in shape. The average kinetic energy of the light and heavy fragments are obtained by momentum conservation. Then, the prompt neutron spectrum in the laboratory system is averaged over the light and heavy fragment contributions.

The physics behind the Los Alamos model is based on averaged fission properties, namely

$$\begin{aligned} &< E_r > && \text{average energy release in fission,} \\ &< E_f^{tot} > && \text{average total kinetic energy of the fragments,} \\ &< E_\gamma^{tot} > && \text{average total energy of prompt gamma-rays,} \\ &< S_n > && \text{average neutron separation energy of the fragments.} \end{aligned} \tag{15}$$

Then, the average fission-fragment excitation energy is given by $< E^* > = < E_r > + E_x - < E_f^{tot} >$, where E_x is the fissioning nucleus excitation energy. For the first-chance photofission, E_x is equal to the incident photon energy. Above the threshold of the second-chance fission (γ, nf), the evaporated neutron energy and its binding energy should be substracted to correctly estimate the residual excitation energy of the fissioning nucleus.

If $< \varepsilon >$ is the average center-of-mass energy of the prompt neutron, then the average neutron multiplicity is given by the energy conservation law

$$\nu_p = \frac{< E^* > - < E_\gamma^{tot} >}{< S_n > + < \varepsilon >}. \tag{16}$$

3. MODELING OF THE DATA

The nuclear reaction models described in section 2 are used to reproduce the experimental data available in the EXFOR database [12]. In this work, TALYS calculations were performed for photoreactions on ^{235}U and ^{232}Th. Prompt fission neutron multiplicity and spectra calculated with the Los-Alamos model are also shown in the case of ^{235}U photofission.

3.1. Uranium-235

3.1.1. Photoabsorption

The GDR parameters used in TALYS for uranium isotopes are from RIPL-2 [13] (cf. Table 1). In the case of ^{235}U, the GDR parameters were adjusted between 9 and 18 MeV onto experimental data by Caldwell *et al.* [14]. Figure 1 shows a comparison between TALYS photoabsorption cross section and experimental data. Caldwell points are given as the sum of measured (γ,n), $(\gamma,2n)$ and (γ,F) cross sections. While Gurevich *et al.* [15] directly measured the total photoabsorption cross section.

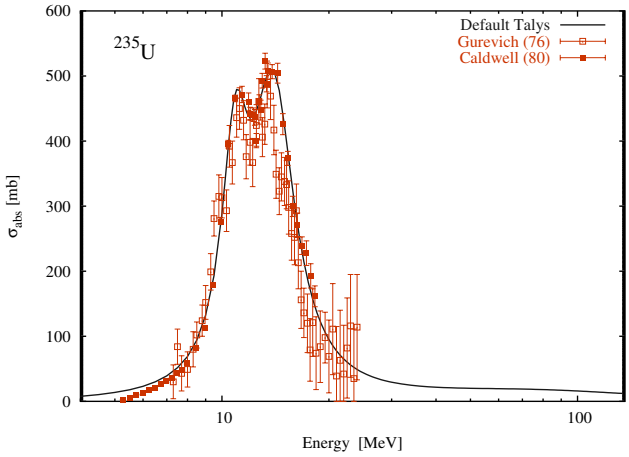

FIGURE 1. ^{235}U photoabsorption cross section: comparison between default TALYS calculation and existing data

3.1.2. Level Density

The level densities calculated using the TALYS code were checked against observed levels at low excitation energy. For the ^{235}U nucleus, the N_{top} parameter was changed from the default value 12 to 29. It led to a slight decrease of the total level density, as shown in Fig. 2. For ^{234}U isotope, N_{top} was changed from 30 to 40 in order to better reproduce the number of experimental levels in the energy region between 1 and 1.5 MeV (see Fig. 2). The default level density values have been used for the ^{233}U isotope.

Calculations were performed with and without changes in ^{233}U, ^{234}U and ^{235}U level densities with no visible effect on calculated photoreaction cross sections.

3.1.3. Neutron Emission

In the present calculations we only used the first three states of the ground state rotational band together with unaltered optical potential parameters from Soukhovitskii *et al.* [10]. Coupling the first three levels (*vs.* five levels) alters the total cross section (n,tot) at incident neutron energies below 0.2 MeV, yet the influence on (γ,n), $(\gamma,2n)$ and (γ,F) cross sections is negligible. In addition ^{234}U+neutron transmission coefficients were also used for ^{233}U+neutron exit channel. This approximation does not affect significantly the calculated cross sections.

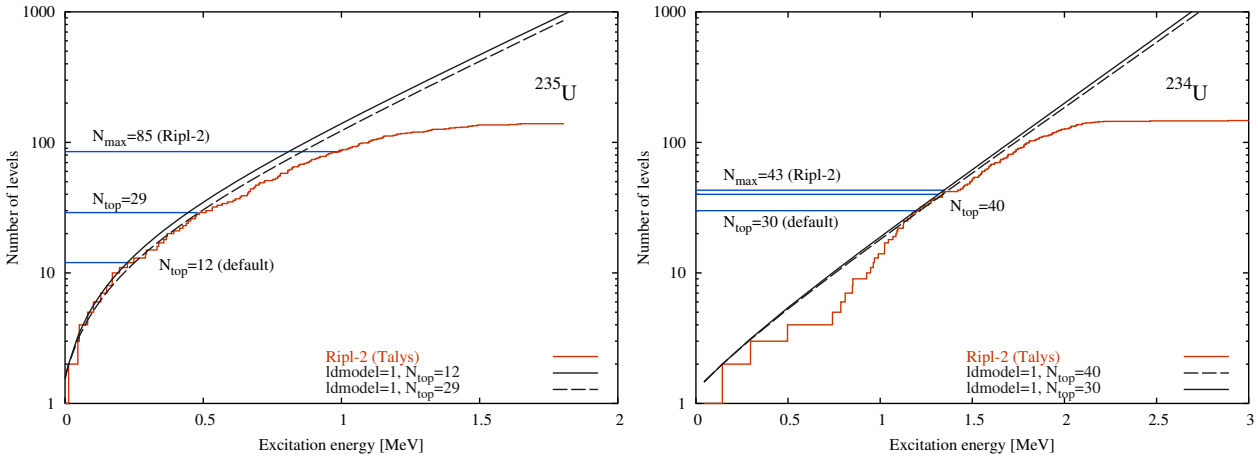

FIGURE 2. Number of levels *vs.* energy in ^{235}U (left) and ^{234}U (right)

For the ^{234}U deformation parameters, we have used interpolated values between ^{233}U and ^{235}U deformations given in the reference [10]. The deformation parameter values used for uranium isotopes are summarized in Table 2.

Calculated neutron total cross sections for ^{233}U and ^{234}U nuclei are compared to the experimental data in Fig. 3. All experimental data are taken from the EXFOR library, where records can be found for ^{233}U from 0.01 to 30 MeV but no information for ^{234}U. Thus, calculated total cross sections of the former nucleus are plotted only up to 30 MeV and total cross sections of the latter are compared to natural uranium data from 0.01 to 130 MeV. For the clarity of the figures some EXFOR entries are not included in the plots. The total cross sections calculated with Soukhovitskii *et al.* optical potential reproduces rather well the experimental data.

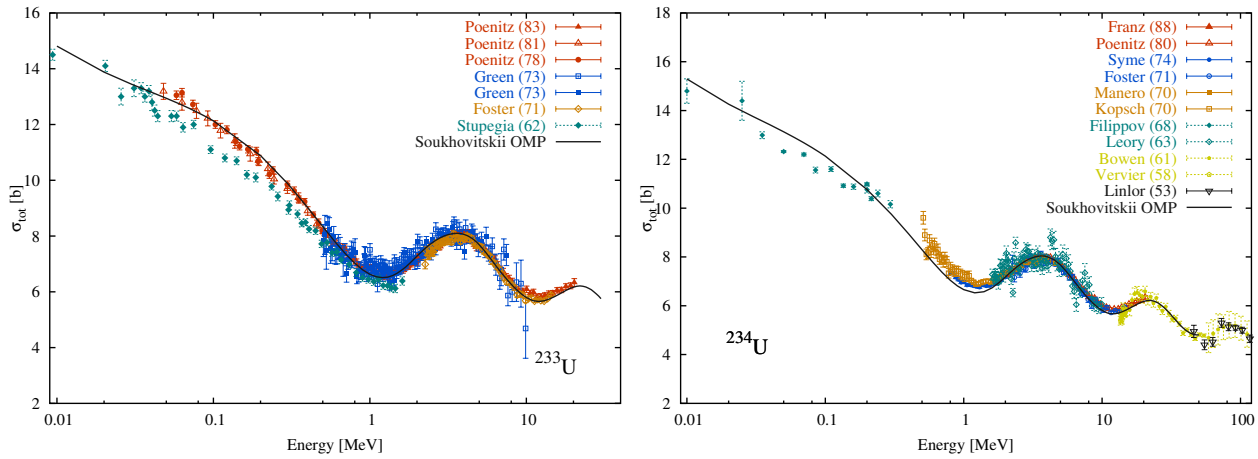

FIGURE 3. Total neutron cross sections of ^{233}U (left) and ^{234}U (experimental data are for ^{nat}U) (right)

3.1.4. Photofission and final results

A number of calculations were done in order to find a set of fission parameters which reproduce Caldwell *et al.* [14] experimental data. The only fission parameters changed in the present calculations are fission barrier heights and widths. Table 3 lists the values obtained in this work together with RIPL-2 data [13]. In addition, the default normalization of the matrix element in TALYS exciton model was fine-tuned to better reproduce the emission of photoneutrons above 12 MeV where pre-equilibrium effects are significant.

Final results are plotted in Fig. 4. The agreement between the cross sections calculated in this work and the experimental data is satisfactory.

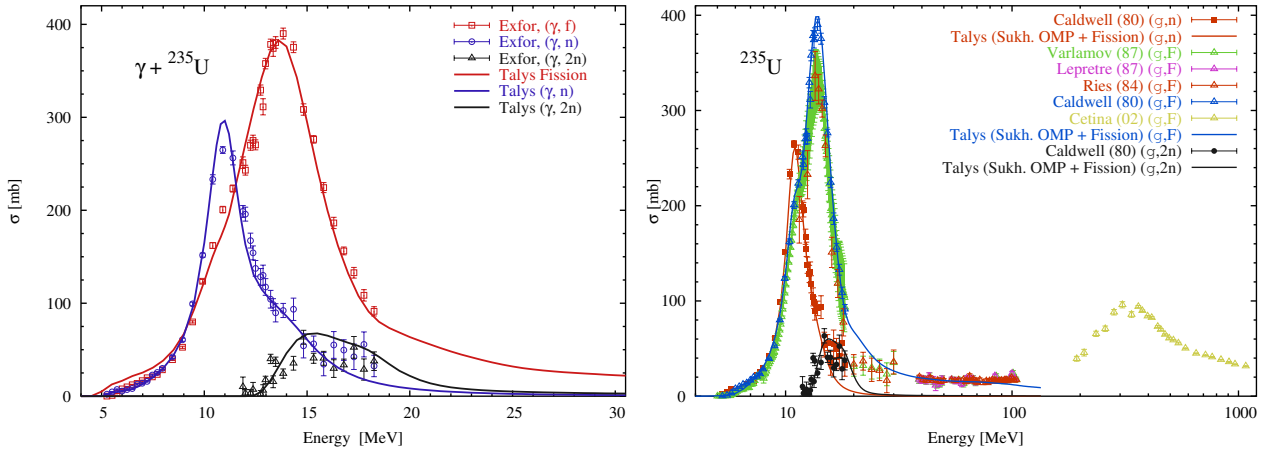

FIGURE 4. ^{235}U (γ,n), $(\gamma,2n)$ and (γ,F) cross sections using Soukhovitskii *et al.* OMP [10] with adjusted fission parameters

On the right part of Fig. 4 calculations are extended up to 130 MeV. Only fission data are available at high energy in the EXFOR database. These data are well reproduced by the quasideuteron model up to 100 MeV. On its right part, Fig. 4 shows, besides Caldwell data, other fission measurements together with Varlamov evaluation. Our calculated total fission cross section is above Varlamov points. In order to reproduce them one would need to alter the selected absorption cross section based on Caldwell *et al.* data [14].

3.1.5. Prompt Fission Neutrons

The Bohr assumption tells us that the compound nucleus decay is independent of its formation. If one further neglects angular momentum effect, both ^{235}U(γ,f) photofission and ^{234}U(n,f) n-induced fission should decay in a similar way. In this work, we have used average parameters (cf. equation 15) from neutron-induced fission to calculate the photofission average neutron multiplicity. As a crude estimate, the same multiple-chance fission probabilities were used for the (γ,f) direct reaction and the (n,f) surrogate reaction. Figures 5 shows preliminary results compared to experimental data from the EXFOR database [12].

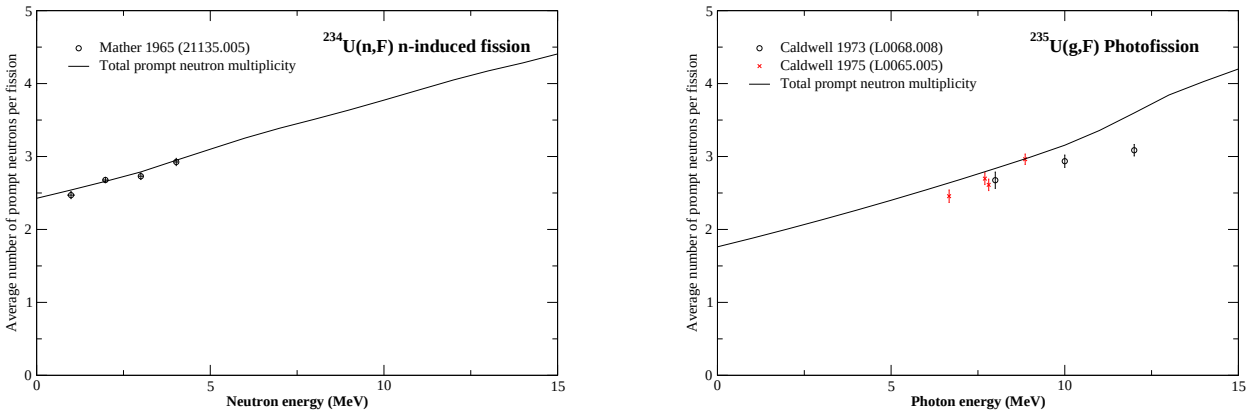

FIGURE 5. Average number of prompt fission neutrons emitted *vs.* incident energy for ^{234}U(n,F) (left) and ^{235}U(γ,F) (right)

3.2. Thorium-232

3.2.1. Photoabsorption

A recent review of photoneutron emission measurements made by Varlamov [16] shows systematic discrepancies between Livermore and Saclay experimental data. In the thorium case, the (γ,xn) cross section measured at Saclay by Veyssiere *et al.* [17] is correct, although there have been compensating effects in (γ,n) and $(\gamma,2n)$ measurements. On the contrary, the ratio $(\gamma,n)/(\gamma,2n)$ measured at Livermore by Caldwell *et al.* [14] is correct and the (γ,xn) cross section should be normalized according to Saclay data.

In this work, the ^{232}Th GDR parameters were adjusted between 9 and 16 MeV to reproduce the corrected photoabsorption cross section proposed by Varlamov. The same GDR parameters were assumed for the ^{231}Th and ^{230}Th isotopes since no experimental data could be found. Table 1 compares the GDR parameters used in this work with parameters from the RIPL-2 database [13].

3.2.2. Level Density

In the case of thorium isotopes the default value ($N_{low} = 2$) used by TALYS to fit the discrete levels at low energy was slightly increased to better reproduce the experimental levels. Therefore, the following TALYS calculations were performed with $N_{low}(^{232}Th) = 5$, $N_{low}(^{231}Th) = 3$, $N_{low}(^{230}Th) = 4$. However, as for ^{235}U modeling, the effect on calculated cross sections was rather small.

3.2.3. Neutron Emission

The transmission coefficients for the ^{231}Th+n exit channel were calculated with the global deformed OMP by Soukhovitskii *et al.* [10] using the same approximation than in the ^{235}U case (see section 3.1.3). The same transmission coefficients were also used for the $(\gamma,2n)$ reaction (i.e. ^{230}Th+n in the exit channel). The deformation parameters published by Soukhovitskii *et al.* [10] have been used for ^{232}Th. The same parameter values were assumed for the quadrupolar and hexadecapolar deformations of ^{231}Th and ^{230}Th (see Table 2).

Calculated neutron total cross sections for ^{231}Th ($T_{1/2} = 26$ hours) are compared to measurements in Fig. 6, where all experimental data actually refer to ^{232}Th. However, there should be little difference between ^{232}Th and ^{231}Th total cross sections above a few MeV. Therefore, the calculated total cross section is in a reasonable agreement with the experimental points.

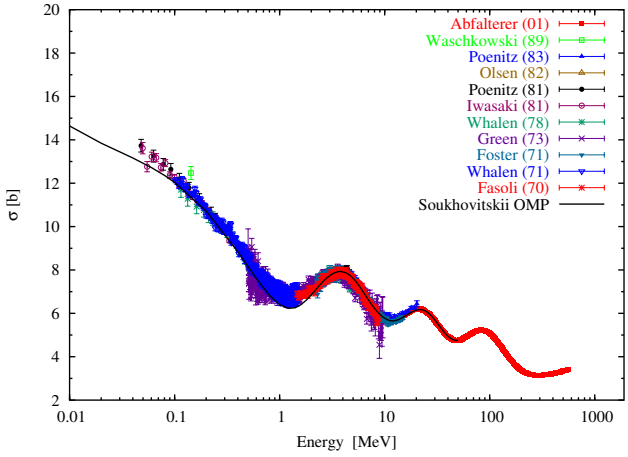

FIGURE 6. ^{231}Th total neutron cross section, experimental data are for the natural element (^{232}Th)

3.2.4. Photofission and final results

There are experimental evidences that the fission barrier of thorium isotopes is more complex than for uranium isotopes. However, we have approximated the fission barriers with a double-humped barrier and ignore the splitting of the outer barrier. Nevertheless, the experimental ^{232}Th photofission cross section was well reproduced as shown on the right part of Fig. 7. In the latter, one compares the calculated total fission (γ,F) cross section with experimental data. The partial fission cross sections (γ,nf) and $(\gamma,2nf)$ are also plotted on the same graph. The presence of a peak in the fission cross section between 6 and 7 MeV is due to 0^- and 1^- transition states located about half-a-MeV above the second fission barrier of ^{232}Th.

The fission barrier heights and curvatures used in this calculation are given in Table 3 for every fissioning nuclei considered in the multiple-chance fission process. On its left part, Fig. 7 shows final cross sections calculated with Soukhovitskii OMP and adjusted fission barrier parameters.

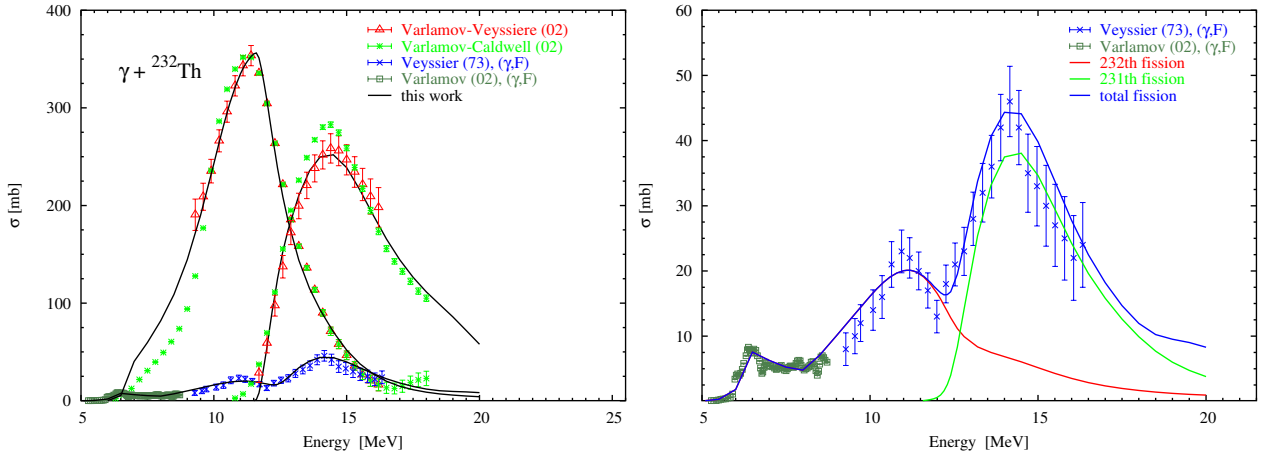

FIGURE 7. Modeling of ^{232}Th cross sections (left) with details of the photofission cross section (right)

4. CONCLUSIONS

^{235}U and ^{232}Th photo-reaction cross sections were calculated with TALYS using a deformed optical potential by Soukhovitskii *et al.* to model the neutron emission. The fission transmission coefficients were calculated using a double humped barrier model. Fission barriers heights and widths were modified to reproduce experimental data. The calculation for ^{232}Th will be extended up to 130 MeV and prompt fission neutron modeling will be continued. The modeling of ^{238}U and ^{239}Pu are also planned in the future. Eventually, these results will be transformed into the ENDF format and proposed to the JEFF project.

ACKNOWLEDGMENTS

The authors whish to thank A. Koning and the TALYS development team (NRG/Petten – CEA/DIF/DPTA/SPN collaboration) for their constant support.

REFERENCES

1. "Handbook on photonuclear data for applications - Cross-sections and spectra", IAEA report, TECDOC-1178, 2000.
2. M-L. Giacri-Mauborgne, *et al.*, *Nucl. Sci. Eng.*, **153**, 33–40 (2006).
3. A. Van Lauwe, *et al.*, this conference.
4. A.J. Koning, S. Hilaire and M.C. Duijvestijn, "TALYS: Comprehensive nuclear reaction modeling", Proc. of the Int. Conf. on *Nuclear Data for Sciece and Technology (ND2004)*, Santa Fe, New Mexico (USA), 2004.

5. D.G. Madland and J.R. Nix, *Nucl. Scien. Eng.*, **81**, 213–271 (1982).
6. M.B. Chadwick, P. Oblozinsky, P.E. Hodgson and G. Reffo, *Phys. Rev. C*, **44**, 814–823 (1991).
7. J.S. Levinger, *Phys. Rev.*, **84**, 43 (1951).
8. A. Gilbert and A.G.W. Cameron, *Can. J. Phys.*, **43**, 1446 (1965).
9. A.V. Ignatyuk, G.N. Smirenkin and A.S. Tishin, *Sov. J. Nucl. Phys.*, **21**, 255 (1975).
10. E.Sh. Soukhovitskii, *et al.*, *J. Phys. G: Nucl. Part. Phys.*, **30**, 905–920 (2004).
11. G. Vladuca and A. Tudora, *Comp. Phys. Comm.*, **125**, 221–238 (2000).
12. *Nuclear Reaction Data Centres Network (NRDC, IAEA)*, 2006, cf. http://www-nds.iaea.org/
13. "Handbook for calculations of nuclear reaction data, RIPL-2", IAEA report, TECDOC-1506, 2006.
14. J.T. Caldwell, *et al.*, *Phys. Rev. C*, **21**, 1215 (1980).
15. G.M. Gurevich, *et al.*, *Nucl. Phys. A*, **273**, 326 (1976).
16. V.V. Varlamov, *et al.*, "Consistent evaluation of photoneutron reaction cross-sections using data obtained in experiments with quasimonoenergetic annihilation photon beams at Livermore and Saclay", IAEA report, INDC(CCP)-440, p.37, 2004.
17. A. Veyssiere, *et al.*, *Nucl. Phys. A*, **199**, 45 (1973).
18. V.M. Maslov, *Nucl. Phys. A*, **743**, 236–255 (2004).

TABLE 1. Giant dipole resonance (GDR) parameters

Nuclei	E_1 [MeV]	σ_1 [MeV]	Γ_1 [MeV]	E_2 [MeV]	σ_2 [MeV]	Γ_2 [MeV]	References
^{235}U	10.90	328.0	2.30	13.96	459.0	4.75	This work, RIPL-2 [13]
^{234}U	11.13	371.0	2.26	13.94	401.0	4.46	This work, RIPL-2 [13]
^{233}U	11.08	221.0	1.94	13.86	433.0	5.47	This work, RIPL-2 [13]
^{232}Th	11.03	302.0	2.71	13.87	449.0	4.77	RIPL-2 [13]*
	11.26	283.0	4.32	14.18	306.0	4.48	RIPL-2 [13]†
	11.18	281.5	4.56	14.23	262.4	4.77	This work
^{231}Th	11.18	281.5	4.56	14.23	262.4	4.77	This work
^{230}Th	11.18	281.5	4.56	14.23	262.4	4.77	This work

* Caldwell, *et al.* [14]
† Veyssiere, *et al.* [17]

TABLE 2. Deformation parameters used with Soukhovitskii *et al.* OMP [10]

Nuclei	β_{20}	β_{40}	β_{60}	References
^{238}U	0.223	0.056	−0.0072	[10]
^{235}U	0.198	0.099	−0.0097	[10]
^{234}U	0.190	0.110	0.001	This work
^{233}U	0.183	0.120	0.003	[10]
^{232}Th	0.206	0.068	−0.002	[10]
^{231}Th	0.2	0.07	—	This work
^{230}Th	0.2	0.07	—	This work

TABLE 3. Fission barrier heights and curvatures

Nuclei	B_{f1} [MeV]	$\hbar\omega_{f1}$ [MeV]	B_{f2} [MeV]	$\hbar\omega_{f2}$ [MeV]	References
^{235}U	5.25	0.7	6.0	0.5	RIPL-2 [13]
^{235}U	5.25	0.5	5.1	0.5	This work
^{234}U	4.80	0.9	5.5	0.6	RIPL-2 [13]
^{234}U	4.80	0.9	5.4	0.28	This work
^{233}U	4.35	0.8	5.55	0.5	RIPL-2 [13]
^{233}U	4.35	0.8	5.25	0.5	This work
^{232}Th	4.8	0.9	6.61	1.2	This work
^{231}Th	6.0	1.2	6.05	0.7	This work
^{230}Th	5.1	0.9	6.85	1.2	Maslov [18]